IEICE TRANS. COMMUN., VOL.E99–B, NO.8 AUGUST 2016

PAPER Special Section on Advanced Information and Communication Technologies and Services in Conjunction with Main Topics of APCC2015

Link-Adaptable Vector-Perturbation ZFBF Precoder for Multi-Point 3D-Beamformers

Masaaki FUJII[†a)], ***Member***

SUMMARY A link adaptation scheme is devised for vector-perturbation (VP) zero-forcing beamforming (ZFBF) MIMO precoding and a link-adaptable VP-ZFBF precoder is applied to multi-point three-dimensional (3D) beamformers to be used in mmWave-band wireless access systems. Channel coding schemes used in current systems, e.g., turbo codes, possess systematic code structures. The VP gain can thus be predicted by searching for perturbation vectors for the symbol vectors mapped from information bits. On the basis of this principle, we constructed an efficient iterative modulation-and-coding-set (MCS) selection procedure for VP-ZFBF precoding. Simulation results demonstrate that our proposed scheme suitably passed on the VP gain to the selection of an appropriate higher-rate MCS index and thus achieved high throughputs by incorporating with multi-point 3D-beamformers.

key words: *antenna array, beamforming, link adaptation, MIMO, precoding, vector perturbation, zero-forcing beamforming*

1. Introduction

The explosive growth of mobile data traffic is leading to demand for large-capacity mobile communication systems. This demand has recently spurred the development of gigabit-class wireless transmission systems. Such high-rate transmission can be supported by using wideband signals accommodated in high carrier frequencies, e.g., quasi-millimeter wave bands. MmWave bands, however, suffer from large propagation losses. High-gain beamforming techniques afforded by massive antenna arrays are therefore key enablers to the practical use of mmWave bands in cellular systems [1].

Analog-digital hybrid beamformers for massive antenna arrays have been investigated for uplink [2] and downlink [3] as practical configurations. To increase average throughputs, many high-gain beamformers need to be densely deployed around user areas so that sufficient received signal power can be secured at users and multiple streams can arrive at users from different directions. By doing this, both high-order spatial multiplexing and high-rate modulation and coding sets (MCS) are expected to become available to achieve high spectrum efficiency.

Zero-forcing beamforming (ZFBF) is well known as a linear MIMO precoding technique based on channel inversion [4]. It, however, suffers from degradation due to channel correlation. To reduce the degradation, a vector-perturbation (VP) technique is applied to ZFBF precoding to significantly improve the transmit power efficiency [5]. In fact, the improvement of throughputs was demonstrated by field experiments [6], but they were limited to fixed MCS. To fully utilize VP gain as throughput improvements, link adaptation is a key to the applicability of VP-ZFBF precoding to practical systems. The VP gain, however, depends on not only instantaneous channels but also data, modulation orders, perturbation variables, and perturbation-vector (PV) search parameters. The exact gain is thus determined after the PV search for channel-coded and modulation-mapped symbol vectors. This makes it difficult to apply channel-adapted MCS selection to VP-ZFBF precoding.

In light of this background, we propose an efficient iterative link adaptation scheme based on systematic code structures. When channel coding is done by using systematic codes such as turbo codes or low-density parity check codes, information bits and parity bits can be separately mapped onto modulation symbol vectors. Starting from MCS selection based on conventional ZFBF precoding, the MCS index is incremented step by step through PV search for the symbol vectors mapped from an initial information bit sequence and then extended information bit sequences. We applied our proposed scheme to multi-point three-dimensional (3D) beamformers and evaluated throughout performances. Simulation results demonstrate that the proposed scheme achieved higher throughputs than conventional ZFBF precoding.

2. System Model

2.1 Multi-Point 3D-Beamformers

Multiple antenna ports equipped with N_A-element planar arrays are de-centrally deployed in cells as shown in Fig. 1. The number of antenna ports is denoted as M_T. This deployment is regarded as a generalized distributed antenna system (GDAS) or large-scale coordinate multi-point (CoMP). In this system, a link budget is secured from an antenna subset that provides a user with small path losses. The subset size is set to N_T ($\leq M_T$). Moreover, the streams transmitted from distributed antenna ports arrive at a user from different arrival angles. The channel matrix is thus more likely to have higher ranks than the one provided with multiple streams transmitted from a single antenna port. The planar array elements are horizontally and vertically partitioned into N_{SA} ($= 2 \times 2$) subarrays for the sake of directivity control [7]. The N_A-dimensional phased-array weight vector steered to

Manuscript received November 10, 2015.
Manuscript revised February 15, 2016.
[†]The author was with Samsung R&D Institute Japan, Yokohama-shi, 230-0027 Japan.
a) E-mail: m.fujii@m.ieice.org
DOI: 10.1587/transcom.2015CCP0001

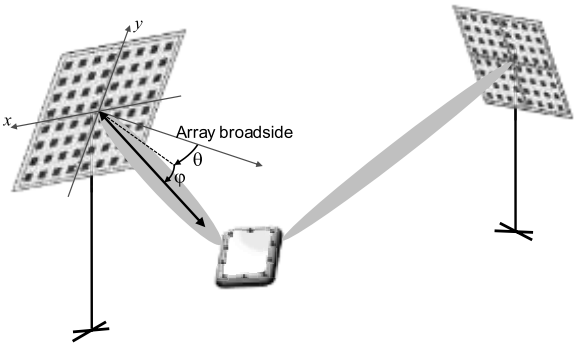

Fig. 1 Multi-point 3D-beamforming.

azimuth and elevation angles (θ_i, φ_i) at frame i at antenna port m is expressed as

$$\boldsymbol{b}_i(m) = \frac{1}{\sqrt{N_A}} \left[\exp\{jd_i(1)\}, \quad \cdots, \quad \exp\{jd_i(N_A)\}\right]^T, \tag{1}$$

where $d_i(n_A)$ is the phase delay to be set at antenna element n_A and is given by

$$d_i(n_A) = -\frac{2\pi}{\lambda}\left(p_{n_A}^{(x)} \sin\theta_i \cos\varphi_i + p_{n_A}^{(y)} \sin\varphi_i\right), \tag{2}$$

where $(p_{n_A}^{(x)}, p_{n_A}^{(y)})$ are positions of antenna element n_A, (θ_i, φ_i) are directions to be steered at elevation and azimuth relative to the broadside of the array, and λ is a wavelength. For the initial setting, one of the N_A orthogonal fixed beam directions that provides the largest array-output signal power is chosen in the uplink. Assuming an L-path model, the L-dimensional subarray-output channel response vectors are estimated for subarray n, and this is denoted as $\hat{\boldsymbol{q}}_i(n)$. The array reference vector is then generated by combing N_{SA} response vectors as

$$\hat{\boldsymbol{q}}_i = \frac{1}{N_{SA}} \sum_{n=1}^{N_{SA}} \hat{\boldsymbol{q}}_i(n). \tag{3}$$

The subarray-output channel response vector is correlated with the array reference vector over L paths:

$$\rho_i(n) = \frac{1}{L} \hat{\boldsymbol{q}}_i^T(n) \hat{\boldsymbol{q}}_i^* = \frac{1}{L} \sum_{l=0}^{L-1} \hat{q}_i(l) \hat{q}_i^*(l). \tag{4}$$

The obtained correlation value is normalized to $\bar{\rho}_i(n)$ with unit power, and the phase shift relative to the array center is extracted as shown in Fig. 2 as

$$\xi_i(n) = Im\{\bar{\rho}_i(n)\}. \tag{5}$$

The slope vector of the quadratic least-squares-error plane is estimated by using $\boldsymbol{\xi}_i = [\xi_i(1), \cdots, \xi_i(N_{SA})]^T$ and an $N_{SA} \times 2$ coordinate matrix $\boldsymbol{A}$ of subarray centers as

$$\boldsymbol{e}_i = \left[e_i^{(x)} \; e_i^{(y)}\right]^T = (\boldsymbol{A}^T \boldsymbol{A})^{-1} \boldsymbol{A}^T \boldsymbol{\xi}_i, \tag{6}$$

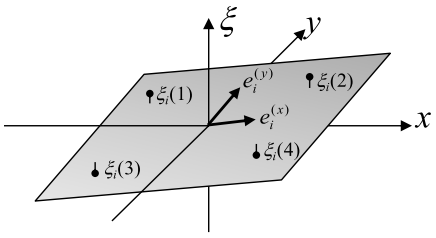

Fig. 2 Phase shift quadratic plane.

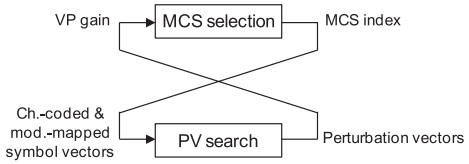

Fig. 3 Interdependent relationship between MCS selection and PV search.

where the entries of $\boldsymbol{A}$ are given for subarray n by

$$\left\{a_x(n), a_y(n)\right\} = \left\{\frac{1}{N_\Lambda} \sum_{n_A \in \Lambda_n} \frac{p_{n_A}^{(x)}}{\lambda}, \frac{1}{N_\Lambda} \sum_{n_A \in \Lambda_n} \frac{p_{n_A}^{(y)}}{\lambda}\right\}, \tag{7}$$

where Λ_n is an antenna element subset for subarray n and N_Λ is the subset size. The directivity control errors are estimated by transforming $\boldsymbol{e}_i$ as

$$\left(\Delta\hat{\theta}_i, \Delta\hat{\varphi}_i\right) = \left(e_i^{(x)}/2\pi\cos\theta_i, e_i^{(y)}/2\pi\cos\varphi_i\right). \tag{8}$$

The beam directions are updated by using a step size parameter μ as

$$(\theta_{i+1}, \varphi_{i+1}) = (\theta_i, \varphi_i) + \mu\left(\Delta\hat{\theta}_i, \Delta\hat{\varphi}_i\right). \tag{9}$$

The phased-array steering vector is then updated from $\boldsymbol{b}_i(m)$ to $\boldsymbol{b}_{i+1}(m)$. Let $\boldsymbol{H}(m)$ be an $N_R \times N_A$ downlink channel matrix between N_R receive antennas and N_A antenna array elements. The effective channel vector is then generated as $\boldsymbol{g}(m) = \boldsymbol{H}(m)\boldsymbol{b}_F(m)$ at frame $i = F$ between the user and antenna port m. The $N_R \times N_T$ effective downlink channel matrix is therefore denoted as $\boldsymbol{G} = \left[\boldsymbol{g}(1) \quad \boldsymbol{g}(2) \quad \cdots \quad \boldsymbol{g}(N_T)\right]$.

2.2 Applicability of VP-MIMO Precoding

The wireless links between N_R receive antennas and N_T beamformers are regarded as $N_R \times N_T$ MIMO channels. The inter-stream interferences are preferably rejected at the transmitter side to curtail the power consumption at the user equipment. For this end, MIMO precoding techniques can be applied to the symbol vectors to be transmitted. A VP technique is well known as a way of improving the transmission performance of linear precoding techniques such as ZFBF precoding. Considering link adaptation, the interdependent relationship between MCS selection and PV search makes it difficult to select an adequate MCS index as illustrated in Fig. 3. The VP gain needs to be estimated

prior to MCS selection to reflect the VP gain to the selection of a higher-rate MCS index. The VP gain is, however, determined after the PV search for channel-coded and modulation-mapped symbol vectors specified by an MCS index. This is the so-called chicken-or-the-egg problem. In addition, the exact VP gain depends on a ZFBF matrix, a coded bit sequence, modulation orders, perturbation variables, and PV search parameters. The theoretical derivation of the exact VP gain is thus considered to be unfeasible. A clue to resolve this issue that we found is as follows. First, information bits and parity bits are separately mapped onto symbol vectors on the basis of systematic code structures to separate the selection of coding rates and modulation orders. Secondly, MCS selection and PV search are alternately carried out in an iterative fashion to find an adequate higher-rate MCS index. The details of the MCS selection procedure that we developed are described in the subsequent section.

3. Iterative MCS Selection Based on Systematic Code Structure

Figure 4 shows a transmitter (T_x) configuration including the MCS selection that we propose. Figure 5 shows a procedure example of generating link-adapted VP symbol vectors through updating an MCS index.

Step 1: *Tentative MCS Selection Based on ZFBF Precoding*

The weight matrix of ZFBF precoding is given by $\boldsymbol{W}_{ZF} = \boldsymbol{G}^{-1}$. The signal vector to be transmitted is assumed to be

$$\boldsymbol{z}(k) = \sqrt{\frac{P}{\gamma_{ZF}}}\boldsymbol{W}_{ZF}\boldsymbol{s}(k), \tag{10}$$

where P is the transmit power, $\boldsymbol{s}(k)$ is the symbol vector to be transmitted at symbol index k, and γ_{ZF} is a normalization factor. The normalization factor is given by

$$\begin{aligned}\gamma_{ZF} &= E\,\|\boldsymbol{W}_{ZF}\boldsymbol{s}(k)\|^2 \\ &= \|\boldsymbol{W}_{ZF}\|_F^2\,,\end{aligned} \tag{11}$$

where $E[\|\boldsymbol{s}(k)\|^2] = 1$ was used and $\|\cdot\|_F$ is the Frobenius norm. The received signal vector is assumed to be

$$\boldsymbol{y}(k) = \boldsymbol{G}\boldsymbol{z}(k) + \boldsymbol{n}(k) = \sqrt{\frac{P}{\gamma_{ZF}}}\boldsymbol{s}(k) + \boldsymbol{n}(k), \tag{12}$$

where $\boldsymbol{n}(k)$ is a noise vector with a variance of σ^2 for each entry. The SINR is estimated as

$$SINR_{ZF} = 10\log_{10}\frac{P}{\gamma_{ZF}\sigma^2}. \tag{13}$$

An MCS index is tentatively selected on the basis of the estimated SINR by referring to an MCS table. The selected MCS index specifies modulation order M, coding rate R, and information bit length N_i (Fig. 5(a)). Note that these parameters are common in all N_T streams because that the channel matrix inversion generates a diagonal channel matrix with the same gains, that is, the same effective SINRs.

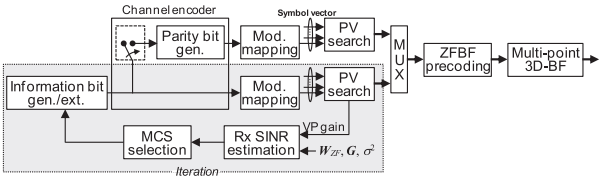

Fig. 4 Transmitter configuration.

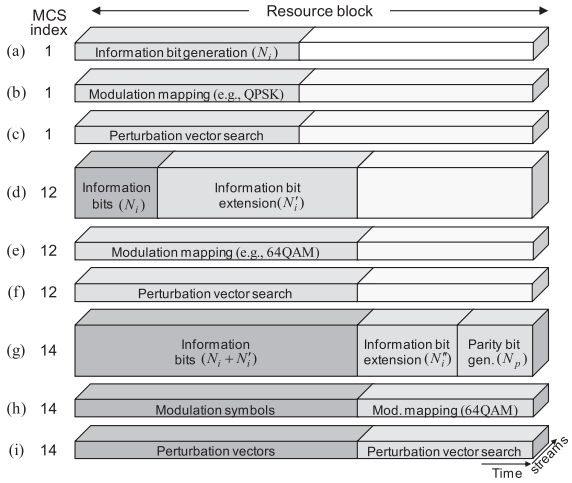

Fig. 5 A procedure example of updating an MCS index and generating VP symbol vectors.

Step 2: *Modulation Mapping and PV Search*

The information bits with length N_i in N_T streams are mapped on modulation symbol vector $\boldsymbol{s}_M(k)$ with modulation order M and with symbol length N_s (Fig. 5(b)). PVs are then searched for in such a way that the squared norm of the precoded signal vector can be minimized as

$$\boldsymbol{l}(k) = \arg\min_{\boldsymbol{l}'}\left\|\boldsymbol{W}_{ZF}\left\{\boldsymbol{s}_M(k) + \tau_M\boldsymbol{l}'\right\}\right\|^2, \tag{14}$$

where τ_M is a perturbation interval for modulation order M and $\boldsymbol{l}'$ is PV candidates (Fig. 5(c)). The perturbation interval of the constellation is chosen as $\tau_M = 2\beta_M(|c_{\max}| + \Delta/2)$, where $|c_{\max}|$ is the absolute value of the constellation symbols with largest magnitude, Δ is the spacing between constellation points, and β_M is an enlargement factor for modulation order M that provides a trade-off between the reduction of modulo arithmetic errors and the VP gain [8]. The larger the modulation order M, the smaller the optimum enlargement factor β_M. As a result, the larger the modulation order used, the larger the VP gain that tends to be provided. This incremental gain for higher order modulations therefore needs to be reflected in the MCS selection. The entry of $\boldsymbol{l}'$ has N_V candidates of perturbation variables. The total number of PV candidates is thus $N_V^{N_T}$. This becomes enormous for practical sizes N_V and N_T. Therefore, the PV is efficiently searched for by using QR-decomposition of $\boldsymbol{W}_{ZF}$ and M-algorithm [9]. Here we use sorted QR-decomposition to more efficiently search for the perturbation vector $\boldsymbol{l}(k)$.

Step 3: *MCS Update, Modulation Mapping, and PV Search*

The signal vector to be transmitted is assumed to be

$$\boldsymbol{z}(k) = \sqrt{\frac{P}{\gamma_{VP}(M)}}\boldsymbol{W}_{ZF}\left\{\boldsymbol{s}_M(k) + \tau_M \boldsymbol{l}(k)\right\}, \tag{15}$$

where $\gamma_{VP}(M)$ is a normalization factor and is calculated as

$$\gamma_{VP}(M) = \frac{1}{N_s}\sum_{k=1}^{N_s}\left\|\boldsymbol{W}_{ZF}\left\{\boldsymbol{s}_M(k) + \tau_M \boldsymbol{l}(k)\right\}\right\|^2. \tag{16}$$

When the PV candidates include the zero vector corresponding to ZFBF precoding (no perturbation), $\gamma_{VP}(M) \leq \gamma_{ZF}$ is guaranteed. The improved SINR is estimated as

$$SINR_{VP}(M) = 10\log_{10}\frac{P}{\gamma_{VP}(M)\sigma^2}. \tag{17}$$

When $SINR_{VP}(M)$ is below the required SNR of the highest coding rate prepared for modulation order M, the subsequent Step 4 will be carried out by setting $M' = M$ and $R' = R$.

When $SINR_{VP}(M)$ exceeds the required SNR of the highest coding rate prepared for modulation order M, the MCS index is updated by referring to the MCS table as $M \rightarrow M'$ and $R \rightarrow R'$. The information bits are extended by length N'_i (Fig. 5(d)) and then mapped onto modulation symbol vectors (Fig. 5(e)). The PVs are newly searched for (Fig. 5(f)) as

$$\boldsymbol{l}(k) = \arg\min_{\boldsymbol{l}'}\left\|\boldsymbol{W}_{ZF}\left\{\boldsymbol{s}_{M'}(k) + \tau_{M'}\boldsymbol{l}'\right\}\right\|^2. \tag{18}$$

The normalization factor is re-calculated as

$$\gamma_{VP}(M') = \frac{1}{N'_s}\sum_{k=1}^{N'_s}\left\|\boldsymbol{W}_{ZF}\left\{\boldsymbol{s}_{M'}(k) + \tau_{M'}\boldsymbol{l}(k)\right\}\right\|^2, \tag{19}$$

where N'_s is the symbol length determined by information bit length $N_i + N'_i$ and modulation order M'. By increasing the modulation order, $\gamma_{VP}(M')$ is likely to be smaller than $\gamma_{VP}(M)$. The SINR is updated as $SINR_{VP}(M')$ and its incremental gain is transformed into the selection of higher coding rates in Step 4.

Step 4: *Coding Rate Update, Parity Bit Generation, Modulation Mapping, and PV Search*

When $SINR_{VP}(M')$ exceeds the required SNR of the coding rate selected at present, the coding rate is updated as $R' \rightarrow R''$. Note that even if $SINR_{VP}(M')$ exceeds the selection boundary of the modulation order, the modulation order will not be further updated so as to keep the complexity low by allowing a small loss due to the selection of a lower MCS index. The information bits are extended by length N''_i. The information bits with total length $N_i + N'_i + N''_i$ are fed into the channel encoder to calculate parity bits with length N_p (Fig. 5(g)). The extended information bits and the parity bits are mapped onto modulation symbol vectors (Fig. 5(h)). The PVs for these symbol vectors are then searched for (Fig. 5(i)) as

$$\boldsymbol{l}(k) = \arg\min_{\boldsymbol{l}'}\left\|\boldsymbol{W}_{ZF}\left\{\boldsymbol{s}_{M'}(k) + \tau_{M'}\boldsymbol{l}'\right\}\right\|^2. \tag{20}$$

The transmit power normalization factor is re-calculated as

$$\gamma'_{VP}(M') = \frac{1}{N''_s}\sum_{k=1}^{N''_s}\left\|\boldsymbol{W}_{ZF}\left\{\boldsymbol{s}_{M'}(k) + \tau_{M'}\boldsymbol{l}(k)\right\}\right\|^2, \tag{21}$$

where N''_s is the symbol length of the resource block. The summation of up to N'_s is already calculated in (19) and thus is utilized for simplicity. The VP-ZFBF-precoded symbol vectors are generated as

$$\boldsymbol{z}(k) = \sqrt{\frac{P}{\gamma'_{VP}(M')}}\boldsymbol{W}_{ZF}\left\{\boldsymbol{s}_{M'}(k) + \tau_{M'}\boldsymbol{l}(k)\right\}. \tag{22}$$

The VP-ZFBF-precoded symbol vector is sent to the multi-point 3D-beamformers.

At the end of this section, we mention the computational complexity. As explained in the procedure by referring to Fig. 5, the PVs searched for QPSK as illustrated in Fig. 5(c) were discarded and thus the computations of searching for the PVs resulted in complexity increase. A possible remedy would be to set a smaller number of survivor paths in M-algorithm in the first PV search.

4. Receiver Structure

Figure 6 shows a receiver (R_x) configuration. The received signal vector is given by

$$\begin{aligned}\boldsymbol{y}(k) &= \boldsymbol{G}\boldsymbol{z}(k) + \boldsymbol{n}(k)\\ &= \sqrt{\frac{P}{\gamma'_{VP}(M')}}\boldsymbol{G}\boldsymbol{W}_{ZF}\left\{\boldsymbol{s}_{M'}(k) + \tau_{M'}\boldsymbol{l}(k)\right\} + \boldsymbol{n}(k)\\ &= \sqrt{\frac{P}{\gamma'_{VP}(M')}}\left\{\boldsymbol{s}_{M'}(k) + \tau_{M'}\boldsymbol{l}(k)\right\} + \boldsymbol{n}(k),\end{aligned} \tag{23}$$

where $\boldsymbol{G}\boldsymbol{W}_{ZF} = \boldsymbol{I}$ was used. At each R_x antenna branch, the received signals are coherently detected. The received signal vector is normalized by the VP gain and then the modulo operation is carried out for the detected symbols as

$$\tilde{\boldsymbol{y}}(k) = \boldsymbol{s}_{M'}(k) + \boldsymbol{n}'(k), \tag{24}$$

where

$$\boldsymbol{n}'(k) = \frac{\boldsymbol{n}(k)}{\sqrt{\frac{P}{\gamma'_{VP}(M')}}}. \tag{25}$$

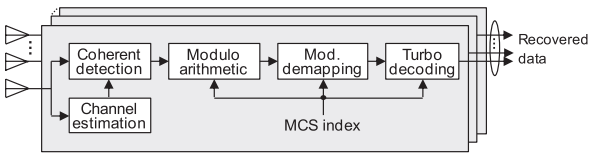

Fig. 6 Receiver configuration.

After that, the recovered symbols are de-mapped into bit-by-bit log-likelihood ratios and are then fed into the turbo decoder to recover the data. Here the feedback of $\boldsymbol{G}$ to the antenna ports is assumed to be perfect. Therefore, the inter-stream interference is assumed to be negligible.

5. Computer Simulations

The throughput performances of the proposed scheme were evaluated under various conditions. Table 1 lists the simulation parameters and Table 2 lists the MCS table in which the indexes are arranged in ascending order of the spectrum efficiencies, that is, the SNRs required to attain a target packet error rate of 1.0×10^{-3}. In the MCS table, 256QAM is included to evaluate potential capabilities although the application of the VP to 256QAM may not be practical. The maximum number of iterations in the proposed MCS selection was set to three as illustrated in Fig. 3.

We used a circular-layout GDAS model [10] as antenna port deployment and user distribution as shown in Fig. 7. We referred to [11] to set up some NLOS parameters. The antenna subset with size N_T was selected as N_T antenna ports with the largest received signal power values in uplink among M_T antenna ports. This can be done by comparing received sounding reference signals in practical scenarios.

The one path model in the resource block corresponds to, e.g., a frequency-domain one-tap channel response in OFDM signals. The channel vector $\hat{\boldsymbol{q}}_i(n)$ in (3) and (4) was thus reduced to a scalar value because of $L = 1$. The channels are assumed to be invariant within the resource block. Throughout the computer simulations, the average packet error rates at the receiver were around 1.0×10^{-3} as targeted.

5.1 Effect of 3D-Beamforming

Figure 8 plots the cumulative distribution function (CDF) of the throughputs provided with the VP-ZFBF precoding when $N_A = 64$ ($N_T = 8$) and 256 ($N_T = 10$), respectively. The dashed lines indicate the throughputs when one of the fixed beams was selected and used. The number of fixed beams used in the simulation set-up was N_A and nearly half of them were not used because the user was located on the ground and thus the array gain was not fully utilized when the user was located off the beam directions. Starting from the selected beam directions, the beam directivity was controlled on the basis of the proposed directivity control scheme in uplink. In (9), the step size parameter μ was

Table 1 Simulation parameters.

Transmit Signals	
Resource block size	480 symbols
Channel coding	Turbo codes
Modulation mapping	Separation mapping for information bits & parity bits
Perturbation variables	0, ±1, ±j1, ±1±j1 ($N_V = 9$)
Enlargement factor for perturbation intervals	1.5 (QPSK), 1.4 (16QAM), 1.3 (64QAM), 1.2 (256QAM)
Number of survivor paths in M-algorithm	81
Target packet error rate	1.0×10^{-3}
Antenna Arrays	
Antenna tilt	6.8 deg.
Array size	$N_A = 64, 144, 256$
Inter-element distance	$D_x = 0.55\lambda$ and $D_y = 0.7\lambda$
Step size parameter in directivity control	$\mu = 0.1$
Channel Model	
Carrier frequency	28 GHz
Antenna port deployment	Circular-layout GDAS model $h = 6$ m, $r_c = 50$ m, $r_u = 40$ m
Number of antenna ports deployed in cell	$M_T = 12$
Number of antenna ports used for transmission	$N_T = 8, 10$
Path loss exponent	3.4
Shadowing deviation	9.8 dB
Path model	1-path 3D channel model (32 sub-paths)
Path angle deviation (azimuth, elevation)	$\sigma_{\delta,\mathrm{BF}} = (0.0,0.0)$ deg. $\sigma_{\delta,\mathrm{user}} = (10.0,10.0)$ deg.
Sub-path offset deviation (azimuth, elevation)	$\sigma_{\Delta,\mathrm{BF}} = (1.0,1.0)$ deg. $\sigma_{\Delta,\mathrm{user}} = (5.0,5.0)$ deg.
Average SNR at center point (w/o array gain)	0.7 dB
Receiver	
Number of Rx antennas	8 or 10 elements deployed on A4 note size
Turbo decoding	Max-log-MAP decoding with 8 iterations
Channel estimation	Ideal at both T_x and R_x

Table 2 MCS table.

Index	Modulation	Coding rate	Required SNR (dB)
0	No transmission		–
1	QPSK	1/2	2.1
2	QPSK	2/3	4.3
3	QPSK	3/4	5.6
4	QPSK	4/5	6.1
5	QPSK	6/7	7.1
6	QPSK	8/9	7.9
7	16QAM	2/3	10.3
8	16QAM	3/4	11.6
9	16QAM	4/5	12.5
10	16QAM	6/7	13.4
11	16QAM	8/9	14.1
12	64QAM	2/3	14.7
13	64QAM	3/4	16.9
14	64QAM	5/6	18.3
15	64QAM	8/9	19.6
16	256QAM	3/4	22.0
17	256QAM	4/5	22.7
18	256QAM	5/6	23.5
19	256QAM	6/7	24.4
20	256QAM	8/9	25.3

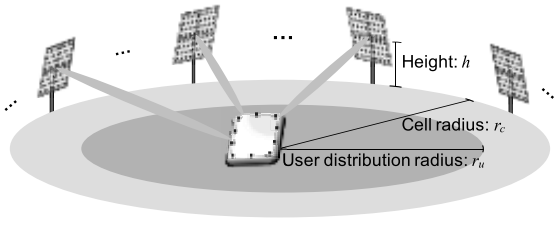

Fig. 7 Circular-layout GDAS model.

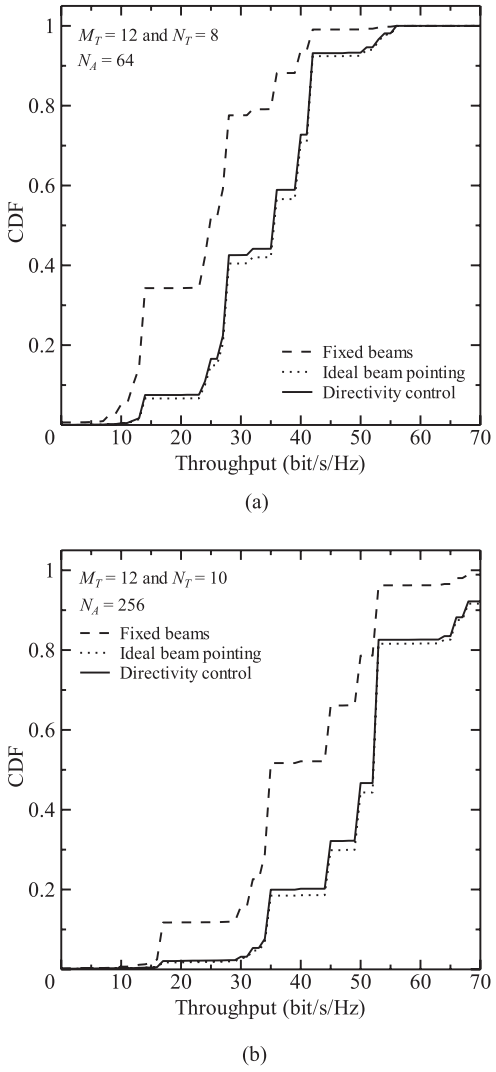

Fig. 8 Effect of 3D-beamsteering on throughputs: (a) $N_T = 8$ and $N_A = 64$ and (b) $N_T = 10$ and $N_A = 256$.

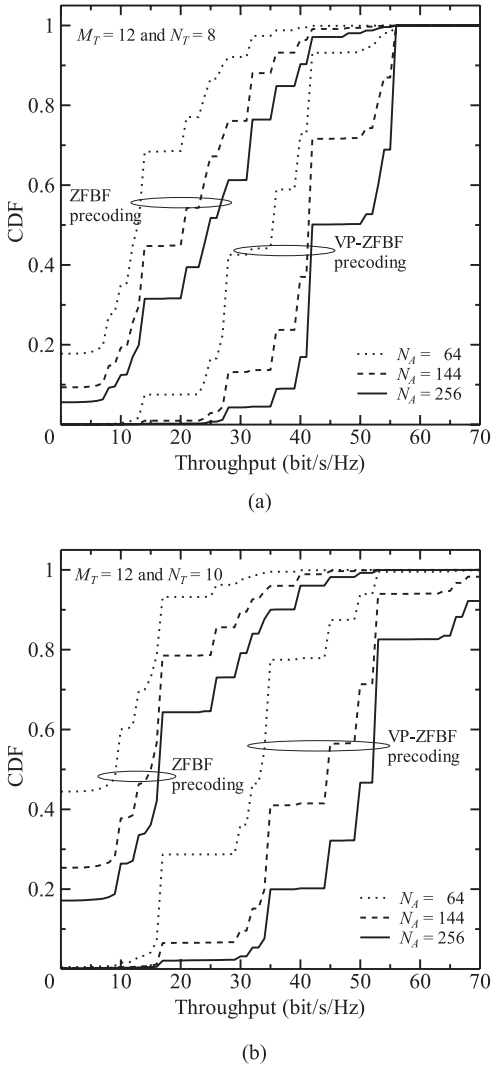

Fig. 9 Throughput comparison between ZFBF precoding and VP-ZFBF precoding: (a) $N_T = 8$ and (b) $N_T = 10$.

set to 0.1, which was optimized in advance to attain high throughputs in the simulation. The number of frames used for the directivity control update was $F = 20$. The resultant steered beams were used for the downlink transmission. As shown in solid lines, the throughputs were significantly improved from those provided with the fixed beams because larger array gains were provided to the user. In addition, the throughputs provided with the directivity control were close to those obtained by the ideal beam pointing (plotted in the dotted line) in which the antenna ports hypothetically know the user direction. This is because the SINR was quantized to 20 levels of MCS even if there was a small gap between SINRs provided with the directivity control and the ideal beam pointing.

5.2 Throughput Comparison with ZFBF Precoding

Figure 9 plots the CDF of the throughputs for $N_A = 64$, 144, and 256 when N_T was 8 and 10. As the array size increased, the throughputs increased because of larger array gains for both the ZFBF precoding and the VP-ZFBF precoding. As shown in both graphs, the VP-ZFBF precoding significantly improved the throughput performances provided with the ZFBF precoding because of the improved transmit power efficiency. Here note that the throughputs provided with the tentative MCS selection in Step 1 in the initial iteration corresponds to the throughputs denoted by ZFBF precoding in the graphs. The MCS updated through the proposed iteration process approaches the near-optimum level for the VP-ZFBF precoding. By setting $N_T = 10$ and $N_A = 256$, the throughputs at CDF = 0.5 were over as high as 50 bit/s/Hz.

The case of $N_T = 10$ provided higher throughputs than the case of $N_T = 8$ because of more streams used for the transmission. When more than two links between the antenna ports and the user suffered from severe channel conditions i.e., low received signal power, however, the throughputs provided with $N_T = 10$ were lower than those provided with $N_T = 8$. In addition, the case of $N_T = 10$ is prone to

provide narrower arrival angle difference between links than the case of $N_T = 8$. This indicates that the dynamic selection of antenna-port subset sizes would further improve the throughputs.

It is worth mentioning that the CDF lines of the VP-ZFBF precoding exhibited *walls* at 14.2, 28.4, and 42.7 bit/s/Hz in Fig. 9(a) and at 17.8, 35.6 and 53.3 bit/s/Hz in Fig. 9(b). These rates correspond to the highest coding rate used in each modulation order. These walls occurred for a way to keep the complexity low as described in Step 4. In other words, the throughputs plateaued at the walls would be further improved and reach the achievable throughputs by setting the maximum number of iterations at four at the expense of the complexity. Further throughout improvement, however, would not be expected by setting the maximum number of iterations at five because the VP gain increase by using a smaller enlargement factor β_M set for higher modulation orders is small compared with the VP gain determined largely by the sizes of N_T and N_V.

6. Conclusion

We proposed a link-adaptable VP-ZFBF precoder and applied it to multi-point 3D beamformers. The iterative MCS selection scheme based on systematic code structures efficiently selected modulation orders and coding rates to sufficiently utilize instantaneous channel conditions and VP gain. In addition, the throughputs over 50 bit/s/Hz were achieved with the CDF of 50% when 10 antenna ports were dynamically selected out of 12 fixed antenna ports equipped with 256-element 3D-beamformers, which were deployed in the circular-layout GDAS model. Our proposed scheme will therefore contribute to increasing throughputs and achieving several ten gigabit/s assuming approximately several hundred MHz∼1 GHz signal bandwidth at mmWave bands.

References

[1] W. Roh, J.-Y. Seol, J. Park, B. Lee, J. Lee, Y. Kim, J. Cho, K. Cheun, and F. Aryanfar, "Millimeter-wave beamforming as an enabling technology for 5G cellular communications: Theoretical feasibility and prototype results," IEEE Commun. Mag., vol.52, no.2, pp.106–113, Feb. 2014.

[2] M. Fujii, J.-Y. Seol, T. Kim, and J. Cho, "Subarray-processing iterartive SISO multi-user detection and multi-beam directivity control for large-scale antenna array," 2013 International Symposium on Intelligent Signal Processing and Communication Systems, pp.596–601, 2013.

[3] T. Obara, S. Suyama, J. Shen, and Y. Okumura, "Joint fixed beamforming and eigenmode precoding for super high bit rate massive MIMO systems using higher frequency bands," 2014 IEEE 25th Annual International Symposium on Personal, Indoor, and Mobile Radio Communication (PIMRC), pp.607–611, 2014.

[4] C.B. Peel, B.M. Hochwald, and A.L. Swindlehurst, "A vector-perturbation technique for near-capacity multiantenna multiuser communication — Part I: Channel inversion and regularization," IEEE Trans. Commun., vol.53, no.1, pp.195–202, Jan. 2005.

[5] B.M. Hochwald, C.B. Peel, and A.L. Swindlehurst, "A vector-perturbation technique for near-capacity multiantenna multiuser communication — Part II: Perturbation," IEEE Trans. Commun., vol.53, no.3, pp.537–544, March 2005.

[6] S. Sonobe, S. Tsukamoto, T. Maeda, K. Yano, H. Ban, M. Uno, and K. Kobayashi, "Field experiments of LTE-Advanced-based 8 × 8 multiuser MIMO system with vector perturbation," WiNMee2013, pp.83–88, Tsukuba Science City, Japan, May 2013.

[7] M. Fujii, J.-Y. Seol, T. Kim, and J. Cho, "Performance comparison between single- and multiple-arrays for 3D-beamsteering multi-user detection," 2014 IEEE 3rd Global Conference on Consumer Electronics (GCCE), pp.90–94, 2014.

[8] H. Mori, Y. Tohzaka, T. Aoki, and Y. Tanabe, "Throughput improvement technique using adaptive control of perturbation interval for downlink multi-user MIMO based on vector perturbation," IEICE Trans. Commun., vol.E95-B, no.9, pp.2861–2869, Sept. 2012.

[9] M. Mohaisen, B. Hui, K. Chang, S. Ji, and J. Joung, "Fixed-complexity vector perturbation with block diagonalization for MU-MIMO systems," 2009 IEEE 9th Malaysia International Conference on Communications (MICC), pp.238–243, 2009.

[10] X. Wang, P. Zhu, and M. Chen, "Antenna location design for generalized distributed antenna systems," IEEE Commun. Lett., vol.13, no.5, pp.315–317, May 2009.

[11] M.K. Samimi and T.S. Rappaport, "Ultra-wideband statistical channel model for 28 GHz millimeter-wave urban NLOS environments," GLOBECOM2014, Austin, TX USA, Dec. 2014.

Masaaki Fujii was born in Hiroshima, Japan. He received the B.S. and M.S. degrees in Communications and Systems from the University of Electro-Communications, Tokyo, Japan, in 1987 and 1989, respectively, and received the Ph.D. degree from Tokyo Institute of Technology, Tokyo, Japan, in 2005. He joined Fujitsu Laboratories Ltd., Kawasaki, Japan, in 1989. During 1995–1998, he was on secondment with YRP Mobile Telecommunications Key Technology Research Laboratories, Co., Ltd., Yokosuka, Japan. He joined Samsung Yokohama Research Institute Co., Ltd. (now Samsung R&D Institute Japan), Yokohama, Japan in September 2002. He is the co-recipient of ICSPAT2000 Best Paper Award and the recipient of MWSCAS2011 Best Paper Award and APCC2015 Best Paper Award.